Carbon Letters (2026) 36:1695–1710
https://doi.org/10.1007/s42823-026-01084-9

ORIGINAL ARTICLE

Platinum-decorated biochar from pequi tree bark as a sustainable catalyst for hydrogen production from ammonia borane

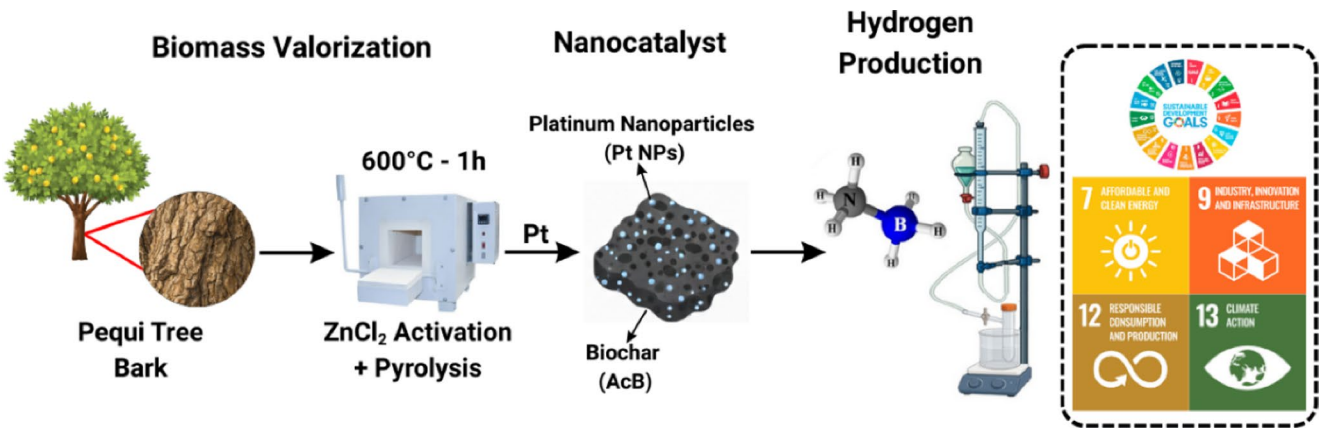
Antonio Machado Netto[1] · Mariele Dalmolin da Silva[2] · Marcela de Oliveira Brahim Cortez[1] · Gessica do Carmo Dias[1] · Bárbara Fernandes de Souza[1] · Guilherme Mateus Bousada[1] · Renata Pereira Lopes Moreira[1]

Received: 3 February 2026 / Revised: 8 May 2026 / Accepted: 18 May 2026 / Published online: 11 June 2026
© The Author(s) 2026

Abstract

Global efforts to mitigate environmental impacts have intensified the demand for cleaner and more sustainable energy systems. Thus, the development of highly efficient and environmentally benign catalysts for hydrogen (H_2) production has emerged as a promising strategy. In this work, a high-performance nanocatalyst composed of platinum nanoparticles supported on activated biochar (Pt NPs/AcB) was developed for hydrogen generation via NH_3BH_3 hydrolysis. The catalytic support was obtained through the valorization of pequi (*Caryocar brasiliense*) peel, an abundant agricultural residue, using pyrolysis followed by chemical activation with $ZnCl_2$. The activation process yielded a material with remarkable textural properties, including a high specific surface area of 1142.43 $m^2\ g^{-1}$ and a predominantly mesoporous structure, which is highly favorable for metal nanoparticle dispersion and anchoring. The Pt NPs/AB catalyst exhibited outstanding catalytic activity toward NH_3BH_3 hydrolysis, achieving a hydrogen generation rate (HGR) of 2982.1 mL $min^{-1}\ g^{-1}$ under optimized conditions (6.5 mmol% Pt, 10 mg of support, 1.00 mL of NH_3BH_3 solution at 0.648 mol L^{-1}, and 30 °C). Mechanistic investigations revealed a primary kinetic isotope effect (KIE) of 6.74, indicating that cleavage of the O–H bond of water is the rate-determining step of the reaction. In addition, the catalyst demonstrated excellent durability, maintaining approximately 100% efficiency over 30 consecutive reaction cycles. Overall, this work presents a robust and sustainable catalytic system that provides an efficient route for on-demand hydrogen generation while highlighting the potential of residual biomass as a precursor for advanced carbon materials in energy-related applications.

Graphical abstract



Keywords Activated biochar · Biomass · Hydrogen · Catalysis · Sustainability

Extended author information available on the last page of the article

1 Introduction

The continuous growth in global energy demand has intensified the reliance on fossil fuels. This dependence has triggered an unprecedented climate crisis driven by the increased emission of greenhouse gases, including carbon dioxide (CO_2), sulfur oxides (SO_x), and nitrogen oxides (NO_x) [1–3]. These emissions play a central role in accelerating global warming. They are also directly associated with the increasing frequency and severity of extreme climatic events, underscoring the urgent need for a transition toward low-carbon, renewable energy systems to ensure long-term environmental sustainability [2].

Against this background, hydrogen (H_2) has emerged as a highly attractive energy vector due to its exceptional gravimetric energy density and environmentally benign combustion profile. Hydrogen exhibits a higher heating value of 142 MJ kg^{-1}, nearly three times that of gasoline, and its oxidation yields water as the sole reaction product, eliminating direct carbon-based emissions [4–6]. These attributes position hydrogen as a strategic component in future energy infrastructures, particularly for applications requiring high energy density, efficient energy conversion, and deep decarbonization.

However, despite its considerable potential, the widespread implementation of hydrogen as a fuel faces major challenges, particularly regarding safe and efficient storage and transportation [1]. Owing to its extremely low density and low volumetric energy density, hydrogen requires extreme storage conditions, such as high-pressure compression (100–400 bar) or liquefaction at cryogenic temperatures (20.37 K) [7]. These approaches are not only highly energy-intensive but also pose significant safety concerns due to the high flammability of H_2 [8].

As an alternative, solid-state hydrogen storage using chemical materials has attracted increasing attention from the scientific community [2, 5, 9–11]. Among these materials, ammonia borane (NH_3BH_3) stands out due to its high hydrogen storage capacity (19.6 wt%), stability under ambient conditions, and non-toxic solid-state nature [12–14].

However, the release of hydrogen from ammonia borane is intrinsically kinetically sluggish and requires the presence of highly efficient catalysts to proceed at rates suitable for practical applications [9]. Historically, noble metals such as platinum, palladium, and ruthenium have exhibited superior catalytic activity toward the dehydrogenation of ammonia borane [15, 16]. Among them, platinum is particularly recognized for its outstanding catalytic efficiency. Nevertheless, the high cost and limited availability of these noble metals constitute major barriers to large-scale implementation, thereby driving research efforts toward strategies that optimize metal utilization and reduce the overall cost of catalytic systems [17, 18].

One of the most effective strategies to enhance the efficiency of metal-based catalysts is their dispersion as nanoparticles on high-surface area support materials [4, 19]. In recent years, biochar has received increasing attention as a catalytic support. Biochar is a carbonaceous material produced by the pyrolysis of residual biomass [20, 21]. Its use as a catalyst support aligns closely with the principles of circular economy and sustainable development [22, 23].

The conversion of agricultural and agro-industrial residues into value-added materials provides an effective solution for waste management while enabling low-cost synthesis routes for advanced carbon materials [22, 23]. Biochar retains the porous structure of the original biomass and can be functionalized with surface organic groups. These features promote strong anchoring and homogeneous dispersion of metal nanoparticles, which are essential for high catalytic performance [19, 22, 23].

Herein, biochar derived from pequi (*Caryocar brasiliense*) peel is evaluated as a support for platinum nanoparticles. Pequi is a native fruit of the Brazilian Cerrado with significant cultural and economic relevance, and its peel is an abundant lignocellulosic byproduct generated by the regional food industry, making it an attractive precursor for porous carbon materials [24]. The central hypothesis of this work is that the intrinsic properties of pequi peel-derived biochar, including its morphology, surface area, and surface functional groups, can promote the formation of ultrasmall and well-dispersed platinum nanoparticles. These characteristics are expected to yield a highly active and stable catalyst for hydrogen production via ammonia borane hydrolysis.

Although numerous studies have investigated activated carbons derived from various biomasses, such as rice husk and sugarcane bagasse, using activating agents like $ZnCl_2$. The resulting physicochemical properties, however, depend strongly on the intrinsic composition of the precursor biomass [25, 26]. In this context, the contents of lignin, cellulose, and minerals (e.g., silica and alkali metals) play a decisive role. These components govern pore formation and the development of surface functional groups, which are critical for the dispersion of active phases and the resulting catalytic performance [25]. Recent studies show that the ash content and mineral composition of biomass strongly influence pyrolysis chemistry. They also affect the final structure of biochars. This includes the role of components such as silica, alkali metals, and alkaline-earth metals [27]. These elements influence the formation of active sites and the thermal stability of the carbon matrix. As a result, materials exhibit surface properties and chemical affinities that vary with the precursor [27].

Moreover, environmental factors such as climate, soil, and cultivation conditions influence the mineral composition of the biomass. This leads to variations in the textural and chemical properties of the activated materials. As a result, different residues do not produce identical carbonaceous catalytic supports after activation [27]. In this context, biochar derived from *Caryocar brasiliense* peel presents a unique organic and inorganic composition. It can promote the development of a tailored pore microstructure and surface chemistry. These features favor the dispersion of active phases and enhance catalytic stability, distinguishing it from other activated carbon precursors [25].

Therefore, this work aims to develop a novel nanocatalyst composed of platinum nanoparticles supported on activated biochar (AcB) derived from pequi (*Caryocar brasiliense*) peel. The key novelty of this study lies in the first-time use of pequi peel–derived biochar as a catalytic support, highlighting how distinct biomass precursors lead to biochars with unique structural and chemical properties. This specificity enables the formation of a highly efficient, stable, and sustainable Pt-based catalyst for hydrogen production via ammonia borane hydrolysis. Comprehensive physicochemical and morphological characterization is combined with a systematic evaluation of catalytic performance, reaction kinetics, and durability, contributing to the development of low-cost, biomass-derived materials for advanced hydrogen storage and generation technologies.

2 Experimental

2.1 Reagents

All reagents used in this work were of analytical grade. These included sodium borohydride (98%, CAS 16940-66-2, NEON), hexachloroplatinic acid (IV) hexahydrate (99.9%, CAS 18497-13-7, Sigma-Aldrich), ammonia borane (95%, CAS 13774-81-7, Sigma-Aldrich), anhydrous zinc chloride (PA grade, CAS 7646-85-7, Êxodo Científica), and hydrochloric acid (37%, CAS 7647-01-0, VETEC). All solutions were prepared using Type II distilled water supplied by a Milli-Q system (Millipore, Bedford, MA, USA).

2.2 Synthesis of biochar from Pequi tree bark

The synthesis of activated biochar (AcB) was based on an adapted method from de Ghani et al. [28] and Faria et al. [29], using pequi (*Caryocar brasiliense*) peel biomass (Figure S1) as the carbon precursor. Initially, 6 g of biomass and 18 g of $ZnCl_2$ were gradually dissolved in 50 mL of Type II water under continuous stirring. To promote effective $ZnCl_2$ impregnation, the homogeneous mixture was dried at 105 °C for 24 h. Subsequently, the dried material was transferred to covered crucibles and subjected to pyrolysis in a muffle furnace at 600 °C for 1 h, using a heating rate of 10 °C min^{-1}. After pyrolysis, the resulting biochar was washed with 0.1 mol L^{-1} HCl under stirring for 1 h. The material was then vacuum-filtered using a 0.45 µm membrane and repeatedly washed with deionized water heated to 80 °C until the supernatant reached neutral pH. Finally, the activated biochar was dried at 60 °C for 24 h.

2.3 Synthesis of platinum nanoparticles decorated with Pequi tree biochar

To synthesize platinum nanoparticles supported on activated biochar (Pt NPs/AcB), 10 mg of AcB were first dispersed in 5 mL of type II water and stirred for 10 min at room temperature (~25 °C). Subsequently, a predetermined volume of an aqueous solution of hexachloroplatinic acid (IV) hexahydrate was added to introduce the platinum precursor, and the suspension was stirred for an additional 10 min. Next, 20 mg of $NaBH_4$ were dissolved in 5 mL of type II water and added dropwise to the system under continuous stirring, which was maintained for a further 10 min to promote in situ reduction of Pt species. The resulting material was then separated by centrifugation at 4000 rpm for 10 min. The supernatant was discarded, and the solid was washed with type II water. This centrifugation–washing procedure was repeated twice to ensure removal of residual reagents.

2.4 Characterization

Scanning Electron Microscopy (SEM) was employed to evaluate the surface morphological and textural characteristics of the biomass and the biochar (AcB). The images were acquired using a scanning electron microscope (JEOL, JSM-6010LA, Japan) equipped with Energy Dispersive Spectroscopy (EDS) for elemental analysis.

The specific surface area and pore characteristics of AcB were determined by N_2 gas adsorption isotherms at 77 K using a surface area and porosity analyzer (Anton Paar, Nova 600, USA). The specific surface area was calculated using the Brunauer–Emmett–Teller (BET) method, while the pore size distribution was obtained by the Barrett–Joyner–Halenda (BJH) method. Prior to analysis, the samples were degassed under vacuum at 100 °C for 3 h to remove surface impurities.

Thermogravimetric analysis (TGA) and differential thermogravimetric analysis (DTG) were performed to evaluate the mass loss of the biomass components and AcB as a function of temperature. First-derivative DTG curves were used to confirm the thermal events observed. The thermograms were recorded using a thermobalance (Shimadzu,

DTG-60 H, Japan) under a nitrogen atmosphere with a constant flow rate of 50 mL min^{-1} and a heating rate of 10 °C min^{-1}, over a temperature range from 20 °C to 800 °C.

Raman spectroscopy analysis was conducted using a micro-Raman spectrometer (Renishaw InVia) equipped with an Nd: YAG laser (λ_0 = 633 nm) and a 50× objective lens (Olympus BX41). The acquisition time for each spectrum was 10 s. Data processing was carried out using Origin 2021 Student, including baseline correction and peak deconvolution. The I_D/I_G ratio was determined from the fitted intensities of the D and G bands.

X-ray diffraction (XRD) analysis was carried out for both AcB and Pt NPs/AcB using a Bruker D8-Discover diffractometer with Cu Kα radiation (λ = 0.1541 nm), over a 2θ range of 10–50°.

Transmission Electron Microscopy (TEM) analysis was performed using a Tecnai G2-20 SuperTwin FEI-200 kV microscope equipped with a silicon–lithium (Si(Li)) detector (EDAX) for Energy-Dispersive X-ray Spectroscopy (EDS) analysis.

Structural characterization was conducted by Fourier Transform Infrared Spectroscopy with Attenuated Total Reflectance (FTIR-ATR) using an ALPHA II spectrometer (Bruker, USA), with a spectral range from 550 to 4000 cm^{-1}. This technique was used to identify the main functional groups present on the AcB support and the NPs-Pt/AcB catalyst.

The elemental composition and oxidation states of the catalyst were determined by X-ray Photoelectron Spectroscopy (XPS). Spectral acquisitions were performed using a Thermo Scientific K-Alpha instrument operating with monochromatic aluminum radiation (Al Kα, 1486 eV).

The platinum content was determined by inductively coupled plasma optical emission spectrometry (ICP-OES) using a Thermo Scientific i-CAP PRO instrument, monitoring the Pt spectral emission line at 224 nm. Samples were digested with 16 mg of material, 6 mL of HCl, and 2 mL of HNO_3 in an Anton Paar Multiwave 3000 microwave oven, heating and maintaining at 180 °C for 15 min.

2.5 Evolution of hydrogen from NH_3BH_3

Freshly prepared Pt NPs/AcB were dispersed in 2.00 mL of type II water in a 10 mL Schlenk tube, which was hermetically sealed with a rubber septum. A rubber hose was connected to the side arm of the Schlenk tube to direct the generated hydrogen gas to a water-filled burette. A schematic representation of the experimental setup is shown in Figure S2. Subsequently, 1.00 mL of an aqueous NH_3BH_3 solution, with concentration adjusted according to the specific assay conditions, was injected into the system using a syringe. The reaction time was continuously monitored. Throughout the experiment, the system was maintained under constant stirring using a temperature-controlled magnetic stirrer.

The pressure (P) exerted by the generated hydrogen gas on the water column was calculated considering the water density (ρ = 1000 kg m^{-3}), gravitational acceleration (g = 9.78 m s^{-2}), local atmospheric pressure (P_0 = 94,258.65 Pa, equivalent to 0.93 atm), and the water column displacement (h), measured in meters. All experiments were conducted at 298.15 K, and the absolute pressure was corrected according to Eq. 1.

$$P = P_0 + \rho * g * h \tag{1}$$

The hydrogen generation rate (HGR) and turnover frequency (TOF) were calculated according to Eqs. 2 and 3, based on the amount of hydrogen produced during the first minute following the addition of the NH_3BH_3 solution to the reaction system.

$$HGR = \frac{\Delta V_{H_2}}{\Delta t * m_{cat}} \tag{2}$$

$$TOF = \frac{P_{atm} * \Delta V_{H_2}}{R * T * n_{Cat} * \Delta t} \tag{3}$$

Where ΔV_{H_2} denotes the variation in hydrogen volume (mL); Δt is the time interval (min); and m_{cat} corresponds to the catalyst mass (g), $\mathbf{P_{atm}}$ is the atmospheric pressure (Pa), R is the gas constant (Pa mL mol^{-1} K^{-1}) and T is the temperature (K), considering only the amount of platinum used in the synthesis of the Pt NPs.

The platinum-catalyzed hydrolysis reaction of ammonia borane, responsible for the release of hydrogen gas, is represented in Eq. 4.

$$NH_3BH_{3(aq)} + 4H_2O_{(l)} \xrightarrow{\text{Catalyst}} NH_4B(OH)_{4(aq)} + 3H_{2(g)} \tag{4}$$

2.6 Evaluation of reaction parameters

A systematic set of experiments was performed to investigate the effects of key reaction parameters on ammonia borane catalytic hydrolysis, including (1) platinum loading in the Pt nanoparticles, (2) activated biochar (AcB) support dosage, (3) NH_3BH_3 concentration, (4) NaOH concentration, (5) kinetic isotope effect (KIE), (6) reaction temperature, and (7) catalyst durability over successive cycles.

The kinetic parameters were determined using the F(C) test function according to the methodology proposed by Bousada et al. (2024).

(1) Platinum loadings of 3.0, 5.0, 6.5, and 8.0 mmol% relative to NH_3BH_3 were investigated using Pt NPs/AcB, under reaction conditions of 10 mg of AcB, 1.00 mL of NH_3BH_3 solution (0.648 mol L^{-1}), and a temperature of 25 °C; a control experiment employing unsupported Pt NPs was also performed.
(2) The effect of support dosage was assessed by varying the AcB mass (10, 15, 20, and 25 mg) while maintaining a constant Pt amount of 0.04212 mmol (6.5 mmol% relative to NH_3BH_3), with reactions carried out at 25 °C using 1.00 mL of NH_3BH_3 (0.648 mol L^{-1}).
(3) The influence of NH_3BH_3 concentration was examined in the range of 0.40–0.74 mol L^{-1}, while keeping the Pt loading.
(4) (6.5 mmol%), AcB mass (10 mg), and temperature (25 °C) constant.
(5) The effect of alkaline conditions was evaluated by replacing type II water with NaOH solutions at concentrations of 0.010, 0.025, 0.050, and 0.075 mol L^{-1} for both catalyst dispersion and NH_3BH_3 dissolution, while maintaining the remaining parameters unchanged.
(6) The kinetic isotope effect was investigated by substituting type II water with deuterium oxide (D_2O) in both the catalyst dispersion and NH_3BH_3 solution; prior to D_2O addition, the catalyst was washed with isopropyl alcohol and vacuum-dried, and the experiments were conducted at 25 °C using 10 mg of AcB, a Pt loading of 6.5 mmol%, and 1.00 mL of NH_3BH_3 (0.648 mol L^{-1}), with the KIE calculated according to Eq. 5.

$$KIE = \frac{k_H}{k_D} \tag{5}$$

Here, k_H represents the kinetic rate constant obtained using H_2O, while k_D corresponds to the rate constant determined using D_2O.

(7) The effect of temperature on hydrogen evolution was evaluated at 25, 30, 40, and 50 °C. All other parameters were kept constant, including 1.0 mL of NH_3BH_3 solution (0.648 mol L^{-1}), a Pt nanoparticle loading of 6.5 mmol%, and 10 mg of activated biochar (AcB). Based on these results, the activation energy (E_a) of the system was determined using the linearized Arrhenius equation (Eq. 6).

$$ln\ (k) = ln\,(A) - \frac{Ea}{R * T} \tag{6}$$

Where k is the reaction rate constant, A is the pre-exponential factor, E_a is the activation energy (kJ mol^{-1}), R is the universal gas constant (J K^{-1} mol^{-1}), and T is the absolute temperature (K).

(8) Catalyst durability was assessed over 30 consecutive reaction cycles under the optimized conditions: 1.0 mL of NH_3BH_3 (0.648 mol L^{-1}), 6.5 mmol% Pt loading, 10 mg of AcB, and 25 °C. At the end of each cycle, a fresh NH_3BH_3 solution (1.0 mL, 0.648 mol L^{-1}) was added directly to the system without washing the catalyst. Every ten cycles, the material was centrifuged and the supernatant removed due to the volumetric limitation of the Schlenk tube used.

3 Results and discussion

3.1 Characterization of materials

The morphological changes induced by biomass carbonization were evaluated by scanning electron microscopy (SEM) (Fig. 1). Prior to activation, the raw biomass exhibited a predominantly flat and compact surface (Fig. 1a). After $ZnCl_2$ treatment, the AcB displayed a markedly fragmented and granular morphology, with the presence of cavities and multilayered structures (Fig. 1b), indicative of significant structural modification. These features are more clearly observed in the higher-magnification image (Fig. 1c). Although SEM does not provide quantitative porosity measurements, the observed morphological transformations suggest increased surface heterogeneity, which is favorable for the anchoring, nucleation, and dispersion of metallic nanoparticles. Such characteristics are highly desirable for catalytic applications, including hydrogen release from NH_3BH_3 [30].

$ZnCl_2$ activation promotes chemical and textural modifications through the introduction of oxygen-containing functional groups and enhanced hydrophilicity, as well as the development of micro- and mesoporous structures. These synergistic effects facilitate the nucleation and stabilization of metallic nanoparticles, contributing to their homogeneous dispersion on the carbonaceous support [31]. Before the catalytic reaction (Fig. 1d), the material retains the fragmented and heterogeneous morphology induced by $ZnCl_2$ activation, characterized by irregular particles and the presence of cavities and interparticle voids. This indicates that the incorporation of Pt does not significantly alter the textural features of the support.

Nitrogen physisorption analysis was performed to evaluate and compare the specific surface area and pore size distribution of the raw biomass and the $ZnCl_2$-activated biochar after chemical activation, which are critical parameters for

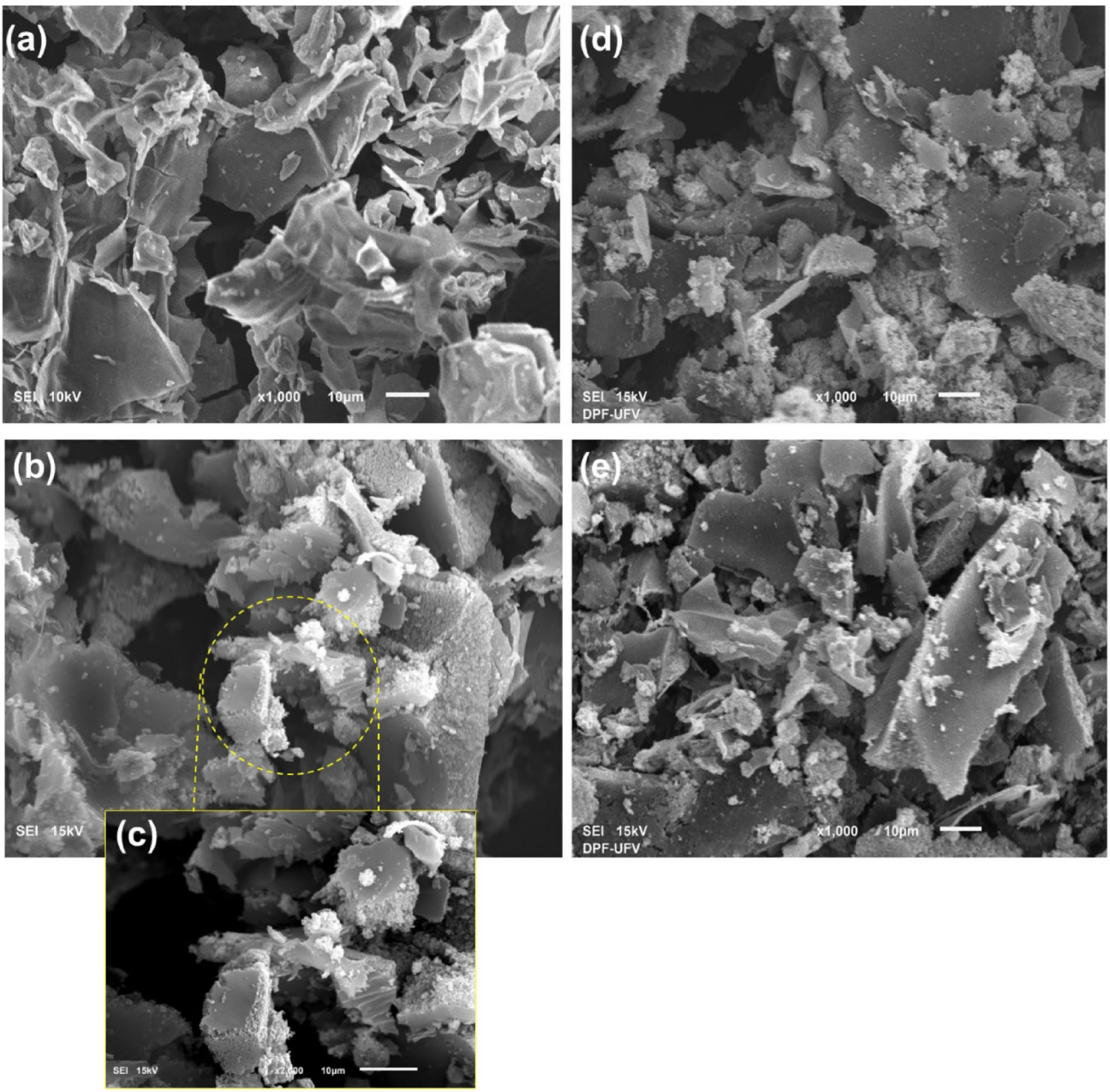


Fig. 1 Scanning electron microscopy (SEM) images of (**a**) pequi (*Caryocar brasiliense*) peel biomass, (**b**) and (**c**) $ZnCl_2$-activated pequi peel biochar (AcB), (**d**) and (**e**) Pt NPs/AcB before and after the evolution of hydrogen from NH_3BH_3, respectively

Table 1 Textural surface characteristics of the pequi (*Caryocar brasiliense*) peel biomass and $ZnCl_2$-activated biochar (AcB)

Sample	Surface area ($m^2\ g^{-1}$)	Pore radius (nm)	Pore volume ($cm^3\ g^{-1}$)
Biomass	0.71	3.28	0.0021
AcB	1142.43	1.72	0.5903

catalytic support applications. The N_2 adsorption–desorption isotherms for the biomass and AcB are shown in Figure S3, while the textural properties, including specific surface area, average pore radius, and total pore volume, are summarized in Table 1.

The results shown in Table 1 demonstrate that $ZnCl_2$ activation had a pronounced impact on the textural properties of the samples. The specific surface area increased dramatically from 0.71 $m^2\ g^{-1}$ for the raw biomass to 1142.43 $m^2\ g^{-1}$ for the activated biochar (AcB). This increase was

accompanied by a 281.1% rise in total pore volume and a decrease in the average pore radius from 3.28 to 1.72 nm, as determined by the Barrett-Joyner-Halenda (BJH) method. These changes confirm the formation of a highly porous structure, dominated by micro- and mesopores, which is particularly suitable for application as a catalytic support [32].

The N_2 adsorption–desorption isotherm of the raw biomass exhibits a profile close to type II (Figure S3a), typical of nonporous or weakly porous materials and generally associated with the presence of macropores [21]. The low surface area and limited pore volume further support this interpretation, indicating a dense and poorly accessible structure [33]. On the other hand, the N_2 adsorption isotherm for AcB (Figure S3b) shows pronounced uptake at low relative pressures, indicative of micropore filling generated during the chemical activation process [34]. Furthermore, the gradual increase in adsorption at higher relative pressures, together with the H4-type hysteresis loop, confirms a well-developed micro–mesoporous structure [35]. The marked increase in adsorbed volume confirms the formation of a well-developed porous structure. Furthermore, the pore size distribution is mainly centered between 2 and 5 nm, confirming the mesoporous nature of the activated material. This feature is highly desirable for catalytic applications, as it facilitates reagent diffusion and promotes the uniform dispersion of metallic species.

Thermogravimetric analysis (TGA) and its derivative (DTG) were employed to assess the thermal stability of the biomass and the activated biochar (BA). As shown in Figure S4, the raw biomass exhibits multiple stages of thermal degradation. An initial mass loss event occurs between 25 and 150 °C, which is attributed to the evaporation of physically adsorbed moisture, light volatiles, and adsorbed hydrocarbons. This behavior is typical of lignocellulosic materials and is commonly associated with the release of physically bound water [36, 37].

In contrast, AcB shows significantly lower mass loss in this temperature range, indicating reduced residual moisture content and enhanced initial thermal stability. At higher temperatures, the biomass undergoes pronounced thermal degradation between 200 and 600 °C, corresponding to the decomposition of hemicellulose, cellulose, and lignin, as evidenced by distinct peaks in the DTG curve [38]. Conversely, AcB displays a markedly more stable thermal profile, characterized by lower degradation rates and the absence of well-defined DTG peaks. This behavior reflects the effective removal of volatile organic components during the carbonization and $ZnCl_2$ activation processes [39]. Overall, these results confirm the superior thermal stability of AcB, a key attribute for catalytic applications involving elevated temperatures and metal nanoparticle deposition. The enhanced thermal robustness ensures structural integrity of the carbon support and promotes the efficient immobilization of metallic species [40].

Raman spectroscopy analysis was performed for both the support and the Pt NPs/AcB, as shown in Fig. 2(a-b). The spectra of both materials exhibit the characteristic D band at 1352 cm^{-1} and G band at 1603 cm^{-1}, which are associated with the structural features of carbon-based materials. The D band is related to structural defects and disorder arising from amorphous carbon domains, whereas the G band

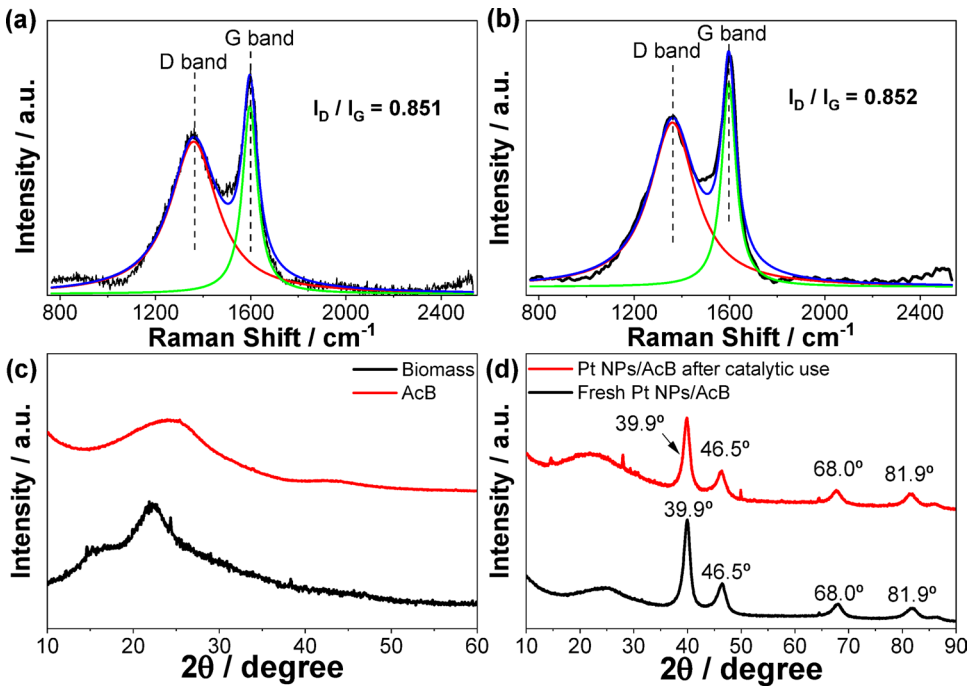


Fig. 2 Raman spectra of (**a**) $ZnCl_2$-activated biochar (AcB) and (**b**) AcB decorated with platinum nanoparticles (Pt NPs/AcB), (**c**) X-ray diffraction (XRD) of biomass and AcB, and (**d**) XRD of Pt NPs/AcB before and after catalytic use

corresponds to graphitic carbon structures [10, 41]. The intensity ratio between the D and G bands (I_D/I_G) was calculated for both samples, yielding values of 0.851 for the biochar and 0.852 for the catalyst. This ratio is commonly used to assess the degree of structural disorder in carbon materials, with lower values indicating a higher degree of graphitic order [42]. The similar I_D/I_G values observed for the biochar before and after platinum deposition indicate that the incorporation of Pt NPs did not significantly alter the carbon structure of the support, thereby preserving its structural integrity.

X-ray diffraction analysis is shown in Fig. 2(c-d). In both materials (biomass and AcB), a broad diffraction feature observed in the 2θ range of 15–30° indicates the predominantly amorphous nature of the biochar, which is associated with the presence of disordered carbon in the support structure [43]. In the catalyst sample, additional diffraction peaks appear at 2θ = 39.9°, 46.5°, 68.0°, and 81.9°, which can be indexed to the characteristic reflections of metallic Pt. These peaks confirm the successful deposition and crystallization of Pt NPs on the biochar surface [44].

Fourier transform infrared (FTIR) spectroscopy was employed to analyze both the biochar support and the catalyst, and the corresponding spectra are shown in Figure S5. In both materials, a broad absorption band centered at 3433 cm^{-1} is observed and assigned to the O–H stretching vibration (ν–OH), which is attributed to surface hydroxyl groups and the hygroscopic nature of biochar, allowing it to absorb moisture from the atmosphere [11, 45]. Additionally, a band at 1593 cm^{-1} is detected, corresponding to the C = C stretching vibration of aromatic compounds present in the carbon framework of the support [21]. A further absorption band around 1226 cm^{-1} is attributed to C–H bending vibrations (γC–H), which are characteristic of aromatic structures in the biochar matrix [46]. The similarity between the FTIR spectra of the biochar and the Pt NPs/AcB indicates that the deposition of platinum nanoparticles does not significantly alter the chemical functionalities of the carbon support.

The deposition of Pt NPs on the AcB was confirmed by TEM, as shown in Fig. 3. As shown in Fig. 3(a), the Pt NPs exhibit a predominantly spheroidal morphology and are well dispersed over the AcB surface, indicating effective impregnation of the support. Figure 3(b) displays well-defined lattice fringes characteristic of metallic nanoparticles, with an interplanar spacing of 0.24 nm. This value can be assigned to the (111) crystallographic plane of face-centered cubic Pt. This assignment is consistent with literature reports for Pt NPs synthesized using similar methods [47]. Figure 3(c) more clearly reveals the presence of nanoparticles, with the particle size distribution shown in Fig. 3(d) and an average size of 5.18 ± 1.44 nm. Comparable values have been reported by Silva de Souza et al. [48], who observed platinum nanoparticles with an average size of 2.80 ± 0.58 nm supported on $LiNbWO_6$.

The EDS results for the biomass and AcB are shown in Figure S6. The biomass exhibits only C and O signals, while the Cu signal originates from the analysis grid. After $ZnCl_2$ activation and pyrolysis, Zn is detected in the material. The EDS spectrum of Pt NPs/AcB (Fig. 3(e)) shows oxygen (53.9 wt%) and platinum (33.8 wt%) as the predominant elements, confirming the presence of Pt nanoparticles on the biochar surface. The remaining signals (C, O, and Zn) are associated with the carbon matrix and residual species from the activation process, while Cu again arises from the TEM grid. Elemental mapping by EDS for C, O, Zn, and Pt in fresh Pt NPs/AcB is shown in Figure S7, indicating a homogeneous distribution of these elements across the material surface.

.

The XPS spectra of the Pt NPs/BA catalyst are presented in Fig. 4. In Fig. 4(a), the XPS survey spectrum is shown, confirming the presence of Zn, Pt, C, O, and N on the surface of the Pt NPs/AcB catalyst. The Zn 2p signals observed at binding energies of 1021 and 1044 eV (Fig. 4(b)) correspond to the Zn $2p_{3/2}$ and Zn $2p_{1/2}$ orbitals, respectively, indicating the presence of Zn^{2+} species originating from the chemical activation of the material with $ZnCl_2$ [49]. The Pt 4f spectrum (Fig. 4(c)) exhibits two characteristic peaks located at 71.3 eV (Pt $4f_{7/2}$) and 74.5 eV (Pt $4f_{5/2}$), which are attributed to metallic platinum (Pt^0), confirming the successful reduction and deposition of Pt NPs on the biochar surface [48]. In addition, the high-resolution spectra of carbon, oxygen, and nitrogen are shown in Figs. 4(d), 4(e), and 4(f), respectively. The C 1 s peak centered at ~285.0 eV is assigned to C–C and C = C bonds, characteristic of graphitic or aliphatic carbon species [50]. The O 1 s signal at ~532.0 eV is attributed to oxygen-containing functional groups, such as C–O bonds and surface hydroxyl species, which are commonly present on activated biochar surfaces [48, 50]. The N 1 s peak centered at ~399.6 eV is associated with nitrogen-containing surface functionalities, including pyrrolic or amine-type nitrogen species (C–N), likely originating from nitrogen-rich reactants and/or surface interactions during catalysis [51]. Overall, the XPS results confirm the successful synthesis of the Pt NPs/AcB catalyst, validating the presence and chemical states of all relevant elements. These findings ensure the reliability of subsequent experiments focused on hydrogen generation from ammonia borane using reduced platinum nanoparticles as the active catalytic phase.

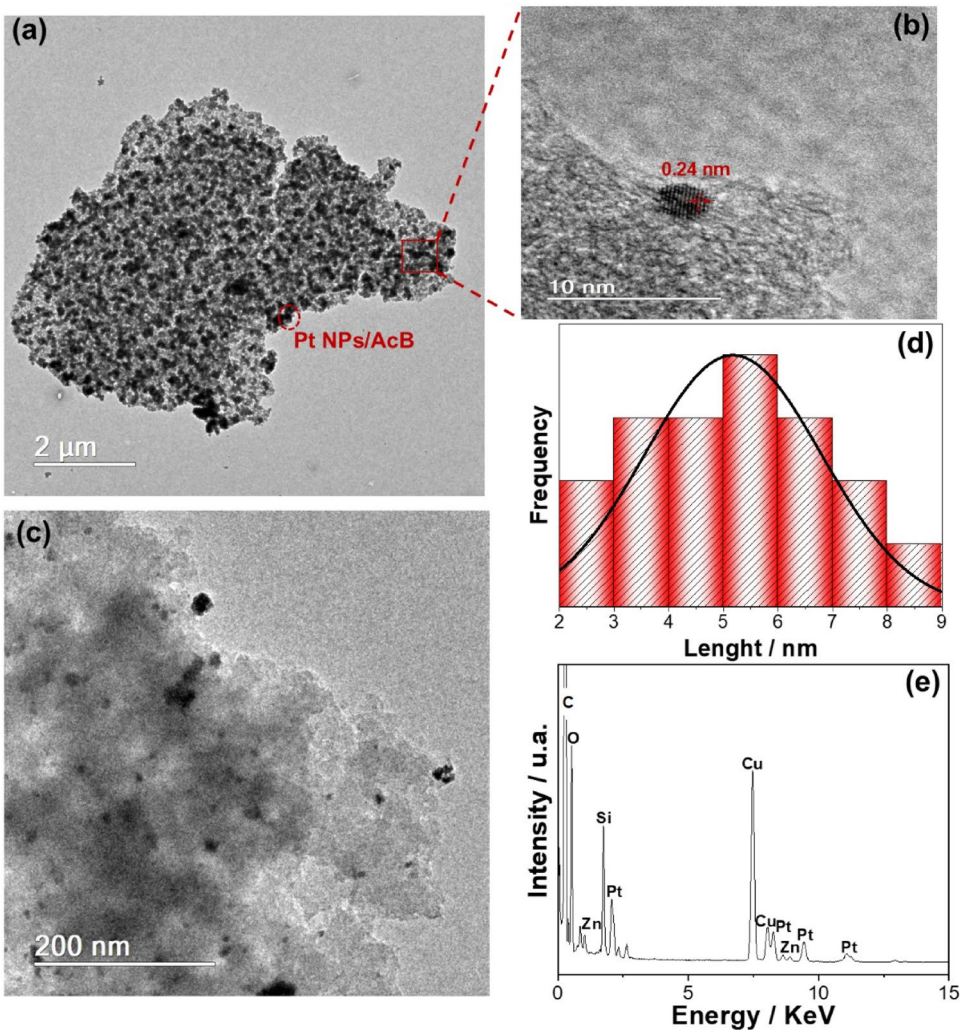


Fig. 3 (**a**) High-resolution transmission electron microscopy (HRTEM) image of Pt nanoparticle–decorated activated biochar (Pt NPs/AcB); (**b**) magnified view of a selected region from (**a**); (**c**) additional high-magnification image highlighting Pt nanoparticles; (**d**) histogram by the particle size distribution; and (**e**) energy-dispersive X-ray spectroscopy (EDS) analysis of Pt NPs/AcB

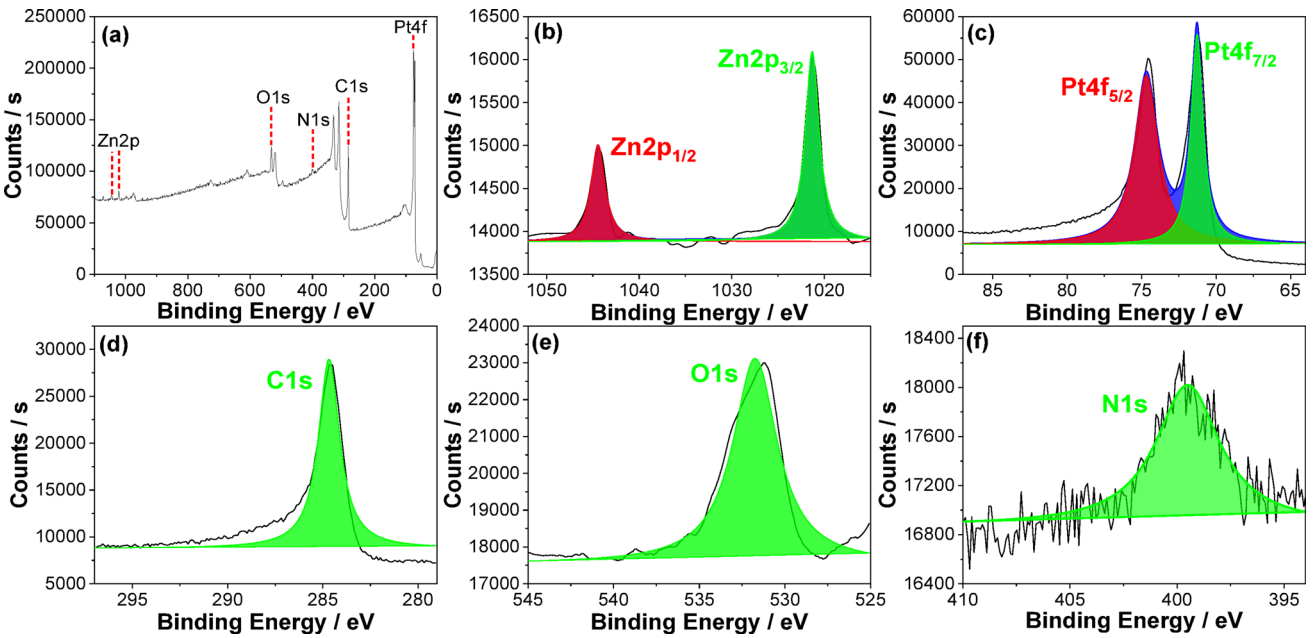


Fig. 4 XPS spectra of Pt NPs/AcB (**a**) survey spectrum, (**b**) Zn 2p, (**c**) Pt 4f, (**d**) C 1 s, (**e**) O 1 s, and (**f**) N 1s

3.2 Application of Pt NPs/AcB for Hydrogen Evolution from Ammonia Borane

3.2.1 Evaluation of platinum loading

The Pt NPs/AcB catalyst was applied to hydrogen evolution from ammonia borane. Initially, the Pt NPs loading was varied, and the corresponding results are shown in Fig. 5. A platinum loading of 3 mol% resulted in a hydrogen generation rate (HGR) of 395.5 mL min^{-1} g^{-1} and a hydrogen yield of 25.5%. In contrast, increasing the platinum loading to 6.5 mol% led to the highest hydrogen generation performance, achieving an HGR of 1781.7 mL min^{-1} g^{-1} and a yield of 85.6%. The favorable reaction kinetics and high hydrogen yield suggest an increased availability of active catalytic sites, as well as an enhanced ability of the catalyst to promote surface renewal during the reaction [11].

Based on the experimental data, kinetic relationships for the hydrolysis of NH_3BH_3 at different catalyst loadings were established (Figure S8), and a plot of the logarithm of the reaction rate constant versus the logarithm of the catalyst dosage is presented in Fig. 5(c). The slope obtained was 4.10, indicating that the reaction exhibits an apparent reaction order higher than pseudo-fourth order with respect to the catalyst loading. This unusual kinetic behavior may be associated with changes in the available surface area of the catalyst, which directly influences the reaction rate. As an illustrative example, a pronounced difference in reaction time was observed between platinum loadings of 5% and 6.5%, with reaction durations of approximately 25 and 5 min, respectively. A similar high reaction order was reported by Bousada et al. [1], who obtained $n = 4.5$ when employing Pt NPs for $NaBH_4$ hydrolysis.

3.2.2 Evaluation of support dosage

The support dosage was varied, and the corresponding results are presented in Figure S9. A support mass of 10 mg provided the best performance, achieving an HGR of 1781.7 mL min^{-1} g^{-1}. It was observed that increasing the amount of AcB used as support led to a decrease in the hydrogen generation rate, indicating that 10 mg remains the optimal reaction condition. Furthermore, a control experiment performed using only the support, without Pt NPs addition, demonstrated the crucial role of this metal as the active catalyst for the dehydrogenation reaction.

3.2.3 Evaluation of different NH_3BH_3 concentrations

The hydrogen production performance obtained from the variation of NH_3BH_3 concentration is shown in Figure S10. It is observed that the concentration of ammonia borane has a significant influence on H_2 generation, exhibiting a positive correlation between the concentration of this hydrogen carrier and the volume of hydrogen produced. A similar behavior was reported by Jiang et al. [52], who investigated the dehydrogenation of NH_3BH_3 using a ruthenium-cobalt-based catalyst.

Despite this overall trend, a decrease in the hydrogen generation rate (HGR) is observed at a concentration of 0.74 mol L^{-1}. This behavior is attributed to a lower initial reaction slope and to the higher mass consumption of platinum, which is directly associated with the use of higher NH_3BH_3 concentrations and directly affects the HGR calculation. The kinetic parameters for reactions at different ammonia borane concentrations are presented in Figure S11. For all concentrations evaluated, the reaction order was approximately pseudo-first order, indicating similar reaction mechanisms across these processes.

3.2.4 Influence of NaOH concentration on hydrogen evolution

The effect of sodium hydroxide concentration on the catalytic hydrolysis of ammonia borane was evaluated to assess the influence of alkaline conditions on hydrogen generation. This study was conducted because the performance of metallic nanoparticles in the hydrolysis of certain hydrogen storage materials can, in some cases, be enhanced by the addition of sodium hydroxide. This effect is attributed to

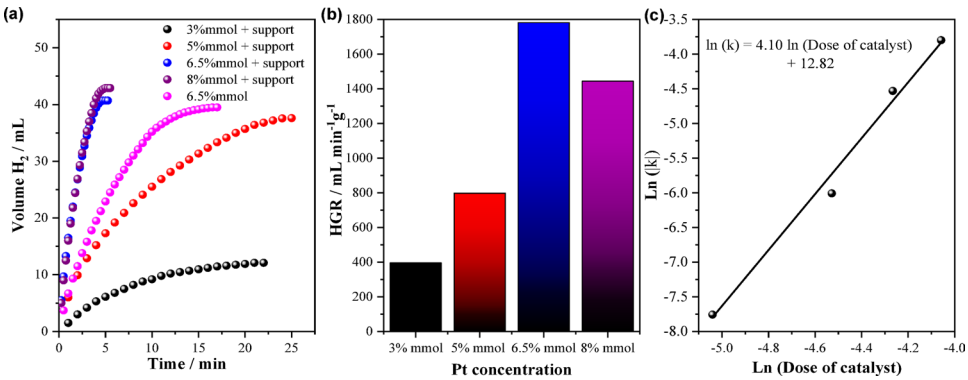


Fig. 5 (**a**) Hydrogen production and (**b**) hydrogen generation rate (HGR) as a function of platinum loading in the NH_3BH_3 hydrolysis reaction mediated by Pt NPs/AcB. (**c**) Determination of the reaction order with respect to catalyst dosage ($R^2 = 0.989$; R^2 adj = 0.984). Reaction conditions: 10 mg of support, 1.00 mL of NH_3BH_3 solution (0.648 mol L^{-1}), and 25 °C

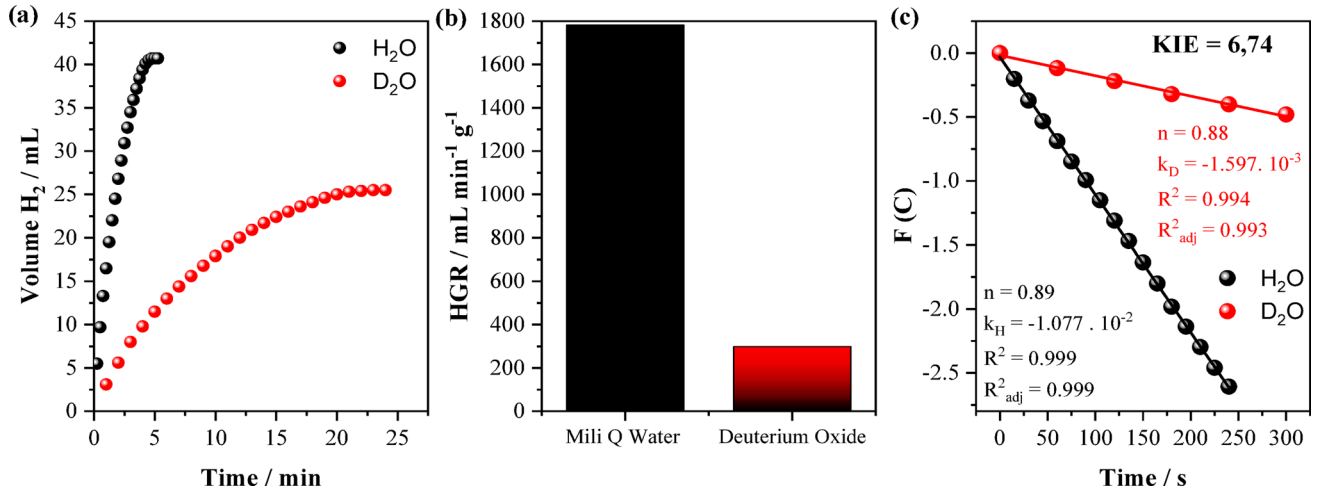


Fig. 6 Kinetic Isotope Effect (KIE) evaluation (**a**) hydrogen production and (**b**) hydrogen generation rate (HGR) using H_2O and D_2O. (**c**) Determination of the KIE based on the calculation of reaction rate constants using the test function method. Reaction conditions: 10 mg of support, 6.5 mmol% of Pt NPs, 1.00 mL of NH_3BH_3 (0.648 mol L^{-1}), and 25 °C

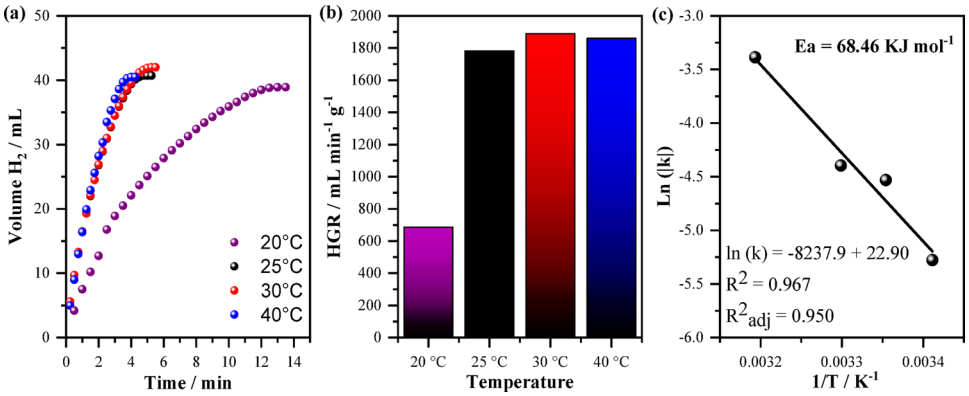


Fig. 7 Evaluation of temperature (**a**) volume of hydrogen produced, (**b**) hydrogen generation rate (HGR) and (**c**) determination of the activation energy based on the Arrhenius plot. Reaction conditions: 10 mg of support, 6.5 mmol% of platinum, and 1.00 mL of NH_3BH_3 (0.648 mol L^{-1})

the coordination of hydroxide anions on the catalyst surface, which increases its electron density and facilitates the oxidative addition of the O–H bond, a key step in metal-mediated hydrolysis reactions [1, 53]. However, as shown in Figure S12, alkalization of the reaction medium led to a reduction in reaction kinetics, resulting in a decrease in the hydrogen generation rate (HGR) of up to 42% at a NaOH concentration of 0.025 mol L^{-1}. A similar trend was reported by Bousada et al. [1], who observed a decrease in reaction rate upon NaOH addition during $NaBH_4$ hydrolysis. This behavior may be attributed to the competitive adsorption of OH^- ions at the active catalytic sites and to the increased solution viscosity, which respectively reduce metal-reactant interactions and hinder mass transfer to the catalytic surface [53, 54].

3.2.5 Kinetic Isotope Effect (KIE) evaluation

The kinetic isotope effect (KIE) was investigated by replacing H_2O with D_2O during NH_3BH_3 hydrolysis, and the comparative results are shown in Fig. 6. KIE analysis is a well-established approach for identifying the rate-determining step of chemical reactions. As shown in Fig. 6(c), a KIE value of 6.74 was obtained, which falls within the range characteristic of a primary isotope effect (2–7), as opposed to a secondary effect (0.7–1.5) [55, 56].

A primary KIE indicates that the cleavage of a bond involving the isotopically labeled atom occurs in the rate-determining step, whereas a secondary KIE reflects more complex mechanistic contributions [11]. Accordingly, the high KIE value demonstrates that the reaction step involving water plays a decisive role in controlling the overall reaction rate. This interpretation is further supported by the fact that hydrolysis performed in D_2O resulted in a reaction time 438% longer and a hydrogen yield 37% lower compared to reactions conducted in H_2O under identical experimental conditions.

3.2.6 Effect of temperature on catalytic performance

The results obtained from the temperature variation experiments are shown in Figs. 7 and S13. An increase in

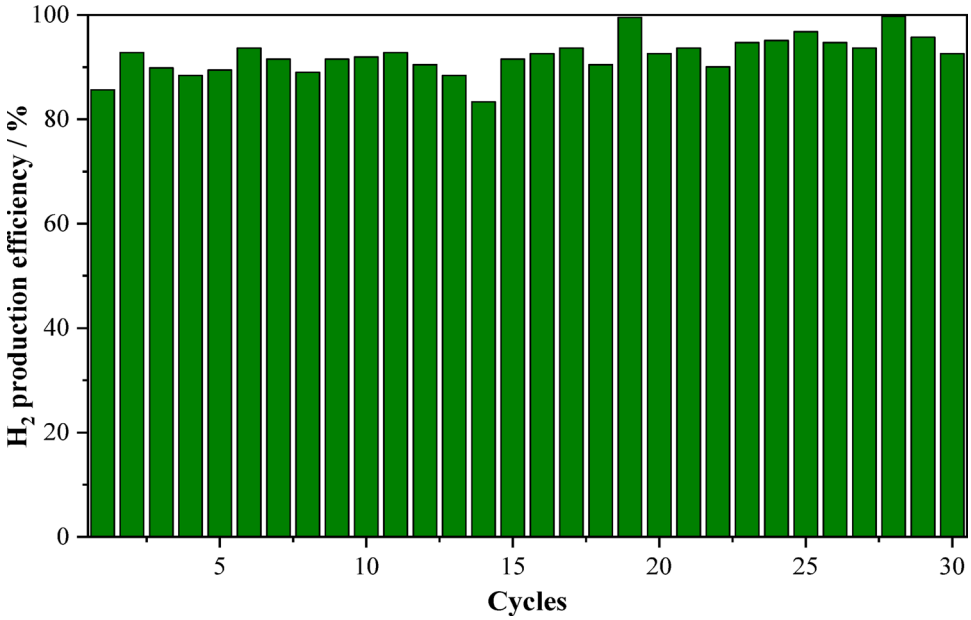


Fig. 8 Hydrogen production efficiency of Pt NPs/AcB over consecutive reaction cycles. Reaction conditions: 10 mg of support, 6.5 mmol% of Pt NPs, 1.00 mL of NH_3BH_3 (0.648 mol L^{-1}), and 25 °C

temperature led to a slight enhancement in reaction kinetics, with the hydrogen generation rate (HGR) increasing to 1888.8 mL min^{-1} g^{-1} compared to 1781.7 mL min^{-1} g^{-1} at 25 °C. Based on these results, the apparent activation energy (E_a) of the reaction was determined to be 68.46 kJ mol^{-1}. This value is consistent with those reported in the literature for NH_3BH_3 hydrolysis catalyzed by noble metals. For instance, Liu et al. [57] and Akbayrak et al. [58] investigated NH_3BH_3 hydrolysis using ruthenium-based catalysts and reported activation energies of 53.6 and 70.0 kJ mol^{-1}, respectively. Moreover, Zhang et al. [59] reported a higher E_a value of 73.5 kJ mol^{-1} for hydrogen production from NH_3BH_3 using a bimetallic platinum-palladium catalyst.

3.2.7 Catalyst durability evaluation

The catalytic stability of the Pt NPs/AcB was evaluated through consecutive reaction cycles, and the efficiency results are shown in Fig. 8. The catalyst exhibited excellent durability, maintaining a high catalytic efficiency of approximately 100% throughout all 30 consecutive reaction cycles. This sustained performance highlights the strong potential of the Pt NPs/BA catalyst for repeated hydrogen generation processes.

To normalize the reaction rate relative to the active Pt content, ICP-OES analysis was performed to determine the actual Pt loading in the catalyst prepared with 10 mg of support and 6.5 mmol% Pt NPs. The results indicated an actual platinum loading of 4.12 ± 0.10 mmol% in the catalyst. This loss of material may be attributed to the washing process during the synthesis of Pt NPs/AcB, as complete settling of the material does not occur. Based on these findings, the hydrogen generation rate (HGR) was normalized to the effective active Pt content, reaching 2982.1 mL min^{-1} g^{-1} at 30 °C. Furthermore, the turnover frequency (TOF) was determined, achieving a value of 1211.5 h^{-1}.

In view of the positive reuse results, additional analyses were performed to evaluate the stability of the material after the reaction. After hydrogen evolution (Fig. 1(e)), the morphology remains essentially unchanged, retaining its rough appearance, which indicates the preservation of the structural integrity and textural properties of the catalyst under the reaction conditions. TEM analysis was performed on the Pt NPs/AcB catalyst after catalytic use, as shown in Figure S14. The material maintained an appearance similar to that observed before use (Fig. 3), with no significant nanoparticle agglomeration, demonstrating the catalyst's stability in line with the durability tests. This result is further supported by the particle size distribution (Figure S4(c)), which yielded an average size of 5.76 ± 1.46 nm, a value close to that found for the fresh Pt NPs/AcB catalyst (5.18 ± 1.44 nm).

The EDS analysis (Figure S14(d)), together with the elemental mapping of Pt NPs/AcB after the reaction (Figure S15), disregarding the copper signal from the grid, confirms the presence of C, O, and Pt distributed throughout the material. The significant presence of Pt highlights the absence of leaching during the catalytic process. The C and O elements are characteristic of the carbonaceous matrix, in agreement with the functional groups identified by FTIR. X-ray diffraction analysis of the fresh catalyst and the catalyst after H_2 evolution is presented in Figs. 2(d). A comparison between the fresh and used catalyst shows that the main diffraction peaks attributed to metallic Pt remain unchanged after the reaction, indicating that the crystalline structure of the nanoparticles is preserved and demonstrating the structural stability of the active phase.

4 Conclusion

This study successfully demonstrated the synthesis and application of a high-performance nanocatalyst composed of platinum nanoparticles supported on activated biochar derived from pequi (*Caryocar brasiliense*) peel (Pt NPs/AcB) for hydrogen production via ammonia borane hydrolysis. The valorization of an abundant agro-industrial residue aligns with circular economy principles and resulted in a carbonaceous support with outstanding physicochemical properties. $ZnCl_2$ activation played a crucial role in developing a mesoporous structure with a remarkably high specific surface area (1142.43 $m^2\ g^{-1}$), which proved essential for the effective anchoring and homogeneous dispersion of Pt NPs, as confirmed by TEM and XRD analyses. The Pt NPs/AcB catalyst exhibited remarkable catalytic activity, achieving a HGR of 2982.1 mL $min^{-1}\ g^{-1}$ under optimized conditions (6.5 mmol% Pt NPs, 10 mg of support, 1.00 mL of NH_3BH_3 at 0.648 mol L^{-1}, and 30 °C), outperforming many catalytic systems reported in the literature. Mechanistic investigation through kinetic isotope effect analysis revealed a primary KIE value of 6.74, indicating that O–H bond cleavage of water is the rate-determining step of the reaction. In addition, the catalyst demonstrated excellent durability, maintaining approximately 100% efficiency over 30 consecutive reaction cycles. Overall, the results not only validate the hypothesis that pequi peel-derived biochar is a promising support for heterogeneous catalysis, but also present a robust, efficient, and sustainable catalytic system for on-demand hydrogen generation. This approach opens new perspectives for the development of low-cost, high-value materials from residual biomass and contributes meaningfully to the advancement of clean hydrogen storage and production technologies. Future studies may explore further optimization of platinum loading and the incorporation of non-noble metals, potentially through alloy formation, to enhance performance and cost-effectiveness.

Supplementary Information The online version contains supplementary material available at https://doi.org/10.1007/s42823-026-01084-9.

Acknowledgements The authors gratefully acknowledge financial support from the Coordination for the Improvement of Higher Education Personnel (CAPES), the National Council for Scientific and Technological Development (CNPq; grant numbers 312400/2021-7, 405828/2022-5, 305649/2021-3, and 407799/2022-2), and the Minas Gerais Research Foundation (FAPEMIG; grants RED-00144-22, APQ-01275-18, and APQ-03572-23). The authors also thank the Departments of Chemistry and Physics at the Federal University of Viçosa for providing access to analytical facilities and technical assistance.

Author contributions Antonio Machado Netto: Conceptualization, Data curation, Formal analysis, Investigation, Methodology, Project administration, Validation, Visualization, and Writing – original draft. Mariele Dalmolin da Silva: Investigation, Formal analysis, Methodology and Writing – original draft. Marcela de Oliveira Brahim Cortez: Investigation, Formal analysis, Methodology and Writing – original draft. Gessica do Carmo Dias: Investigation, Methodology, and Writing – original draft. Bárbara Fernandes de Souza: Methodology, and Formal analysis. Guilherme Mateus Bousada: Methodology, and Formal analysis. Renata Pereira Lopes Moreira: Conceptualization, Supervision, and Writing—review and editing. All authors have read and agreed to the published version of the manuscript.

Funding The Article Processing Charge (APC) for the publication of this research was funded by the Coordenação de Aperfeiçoamento de Pessoal de Nível Superior - Brasil (CAPES) (ROR identifier: 00x0ma614). This work was supported by the Fundação de Amparo à Pesquisa do Estado de Minas Gerais (FAPEMIG, grants RED-00144-22, APQ-01275-18, and APQ-03572-23).

Data availability All data supporting the findings of this study are included within the manuscript.

Declarations

Competing Interests The authors declare no conflicts of interest.

Declaration of AI-Assisted Technologies During the preparation of this manuscript, ChatGPT was used solely for language editing, grammatical revision and in assisting with the preparation of Figure S1. All scientific concepts, interpretations, and technical conclusions are entirely the responsibility of the authors.

Open Access This article is licensed under a Creative Commons Attribution 4.0 International License, which permits use, sharing, adaptation, distribution and reproduction in any medium or format, as long as you give appropriate credit to the original author(s) and the source, provide a link to the Creative Commons licence, and indicate if changes were made. The images or other third party material in this article are included in the article's Creative Commons licence, unless indicated otherwise in a credit line to the material. If material is not included in the article's Creative Commons licence and your intended use is not permitted by statutory regulation or exceeds the permitted use, you will need to obtain permission directly from the copyright holder. To view a copy of this licence, visit http://creativecommons.org/licenses/by/4.0/.

References

1. Bousada GM, Nogueira Da Silva V, Fernandes De Souza B, De Oliveira RS, Machado I Junior, Da Cunha CHF et al (2024) Niobic acid as a support for microheterogeneous nanocatalysis of sodium borohydride hydrolysis under mild conditions. RSC Adv 14:19459–71. https://doi.org/10.1039/D4RA01879F
2. Coelho LO, Sperandio GH, Chagas Da Silva R, Lopes Moreira RP, De Jesus JR (2024) Niobium metal–organic framework is an efficient catalytic support for the green hydrogen evolution process from metal hydride. Processes 12:2342. https://doi.org/10.3390/pr12112342
3. Lorenzini L, Anunciação MG, Gomes IB, Silva RCF, Silva TA, Moreira RPL et al (2025) Incorporation of Co and Ni nanoparticles into sustainable mesoporous carbons for hydrogen evolution from sodium borohydride. Int J Hydrog Energy 135:382–92. https://doi.org/10.1016/j.ijhydene.2025.05.025
4. Dos Reis TM, Alves ACDC, Da Silva VN, Siqueira GO, De Andrade FV, De Lima GM et al (2024) Synthesis of ecofriendly

bimetallic Pt/Ni nanoparticles on KNbO3 via hydrothermal process for sustainable hydrogen evolution from NaBH4. Processes 12:2340. https://doi.org/10.3390/pr12112340
5. Junior IM, Sperandio GH, Lopes RP (2024) Efficient hydrogen evolution from NaBH4 using bimetallic nanoparticles (Ni–Co) supported on recycled Zn–C battery electrolyte paste. Int J Hydrog Energy 53:1323–1331. https://doi.org/10.1016/j.ijhydene.2023.11.362
6. Ferreira M, Dias G MC, Andradre A, Machado Junior T, Marques Neto IO, Silva JS (2025) Cobalt-Nickel Nanocatalyst Supported on Phosphorus-Doped Hydrochar from Malt Bagasse Waste Synthesized via One-Pot Wet Pyrolysis for Safe and Sustainable Hydrogen Fuel Evolution from Sodium Borohydride. J Braz Chem Soc. https://doi.org/10.21577/0103-5053.20250127
7. Dos Santos JL, Machado Junior I, Sperandio GH, Do C, Dias G, Dias A, De Lima M (2025) Platinum and other Metals Doped-Manganese Tungstate as a Novel Catalytic Support for NaBH4 Hydrolysis and Hydrogen Evolution Under Mild Conditions. J Braz Chem Soc. https://doi.org/10.21577/0103-5053.20250113
8. Squizzatto EP, Andrade TDA, Lopes Moreira RP, Guimarães LDM, Da Silva MJ, Novaes FJM et al (2024) Development of a Niobium-based coordination compound with catalytic applications for green hydrogen evolution. Processes 12:2677. https://doi.org/10.3390/pr12122677
9. Cao Y, Yang S, Liu P, Zhu Q, Zheng X (2025) Nickel-promoted ruthenium nanocatalysts for controllable hydrogen production from NH3BH3 hydrolysis. Appl Surf Sci 688:162345. https://doi.org/10.1016/j.apsusc.2025.162345
10. Souza EIP, Favero UG, Sperandio GH, Andrade TA, Moreira RPL, Hespanhol MC (2025) Sustainable nanocatalyst synthesized from battery waste for enhanced hydrogen evolution: A circular economy approach. J Environ Chem Eng 13:116283. https://doi.org/10.1016/j.jece.2025.116283
11. Sperandio GH, De Carvalho JP, De Jesus CBR, Junior IM, De Oliveira KLA, Puiatti GA et al (2024) Hydrogen evolution from NaBH4 using novel Ni/Pt nanoparticles decorated on a niobium-based composite. Int J Hydrog Energy 83:774–83. https://doi.org/10.1016/j.ijhydene.2024.07.022
12. Çetin MB, Top T, Yurderi M, Zahmakıran M, Rakap M (2024) Tungsten(VI) oxide-supported nickel/silver nanoparticles for photocatalytic hydrogen evolution from ammonia-borane. Int J Hydrog Energy 72:60–73. https://doi.org/10.1016/j.ijhydene.2024.05.361
13. Shimizu Y, Miyagi A, Tripathi AK, Nakagawa T (2024) Delayed ammonia release of ammonia borane hydrolysis by citric acid. Int J Hydrog Energy 82:733–739. https://doi.org/10.1016/j.ijhydene.2024.07.435
14. Zhao H, Liu Y, Zhang W, Peng X, Tang Q, Ding Q et al (2024) NiPdMo nanoparticles reduced by Cs[closo-B6H7] as high-performance catalysts for hydrogen generation from hydrolysis of ammonia borane. Int J Hydrog Energy 60:451–7. https://doi.org/10.1016/j.ijhydene.2024.02.232
15. Chandra M, Xu Q (2006) A high-performance hydrogen generation system: transition metal-catalyzed dissociation and hydrolysis of ammonia–borane. J Power Sources 156:190–4. https://doi.org/10.1016/j.jpowsour.2005.05.043
16. Jiang W, Fu C, Li G, Zhang S, Xu D, Li L (2024) Theoretical Investigation on the Catalytic Performance of g-C_3N_4 Supported Single Metal Atom Catalysts for Hydrogen Evolution from NH_3BH_3. Organometallics 43:48–54. https://doi.org/10.1021/acs.organomet.3c00347
17. Guan S, Yuan Z, Zhao S, Zhuang Z, Zhang H, Shen R et al (2024) Efficient hydrogen generation from ammonia borane hydrolysis on a tandem Ruthenium–Platinum–Titanium catalyst. Angew Chem Int Ed Engl 63:e202408193. https://doi.org/10.1002/anie.202408193
18. Uzundurukan A, Devrim Y (2019) Carbon nanotube-graphene hybrid supported platinum as an effective catalyst for hydrogen generation from hydrolysis of ammonia borane. Int J Hydrog Energy 44:26773–26782. https://doi.org/10.1016/j.ijhydene.2019.08.153
19. Campisi S, Chan-Thaw CE, Villa A (2018) Understanding Heteroatom-Mediated Metal–Support Interactions in Functionalized Carbons: A Perspective Review. Appl Sci 8:1159. https://doi.org/10.3390/app8071159
20. De Oliveira Fontoura CR, Dutra LV, Guezgüan SM, Nascimento MA, De Oliveira AF, Lopes RP (2022) Optimization of one-pot H3PO4-activated hydrochar synthesis by Doehlert design: characterization and application. J Anal Appl Pyrolysis 168:105775. https://doi.org/10.1016/j.jaap.2022.105775
21. Silva A, Bousada GM, Mazzini LFM, Guezguan SM, De Freitas CPM, Monteiro KA et al (2024) Biochar from malt residue: toward a circular economy for sustainable fluoroquinolone removal in aqueous systems. J Anal Appl Pyrolysis 183:106707. https://doi.org/10.1016/j.jaap.2024.106707
22. Rizwan M, Eisa MH, Zada A, Azizi S, Alkaoud AM, Albishi MS et al (2025) Cutting edge advancements in biochar applications: thermochemical, fermentative, photocatalytic and electrocatalytic hydrogen production and storage. Fuel 402:136016. https://doi.org/10.1016/j.fuel.2025.136016
23. Yan K, Yang X, Yuan Q (2025) Biochar for carbon-negative hydrogen production from fossil fuel reservoirs. J Clean Prod 512:145463. https://doi.org/10.1016/j.jclepro.2025.145463
24. Silva MD, Moreira RPL, Rosa AP, Borges AC (2025) Optimization of microwave-assisted extraction of tannins and phenolic compounds obtained from the pequi tree (*Caryocar brasiliense*). Chem Eng Process Process Intensif 217:110462. https://doi.org/10.1016/j.cep.2025.110462
25. Merum D, Kang M (2025) From biomass to energy storage: sustainable carbon materials for next-generation supercapacitors. Adv Ind Eng Chem 1:26. https://doi.org/10.1007/s44405-025-00028-7
26. Dheyab MA, Oladzadabbasabadi N, Aziz AA, Khaniabadi PM, Al-ouqaili MTS, Jameel MS et al (2024) Recent advances of plant-mediated metal nanoparticles: synthesis, properties, and emerging applications for wastewater treatment. J Environ Chem Eng 12:112345. https://doi.org/10.1016/j.jece.2024.112345
27. Puri L, Hu Y, Naterer G (2024) Critical review of the role of ash content and composition in biomass pyrolysis. Front Fuels 2:1378361. https://doi.org/10.3389/ffuel.2024.1378361
28. Ghani ZA, Yusoff MS, Zaman NQ, Zamri MFMA, Andas J (2017) Optimization of preparation conditions for activated carbon from banana pseudo-stem using response surface methodology on removal of color and COD from landfill leachate. Waste Manag 62:177–87. https://doi.org/10.1016/j.wasman.2017.02.026
29. Faria MDSL, Lima RMR, Superbi De Sousa RDC, Carraro Borges A (2025) Phosphate adsorption study employing a synthesized activated carbon derived from banana pseudostem. Rev AIDIS Ing Cienc Ambient 111–124. https://doi.org/10.22201/iingen.0718378xe.2025.18.1.88930
30. Santos JL, Megías-Sayago C, Ivanova S, Centeno MÁ, Odriozola JA (2021) Functionalized biochars as supports for Pd/C catalysts for efficient hydrogen production from formic acid. Appl Catal B Environ 282:119615. https://doi.org/10.1016/j.apcatb.2020.119615
31. Macchi S, Denmark I, Le T, Forson M, Bashiru M, Jalihal A et al (2021) Recent advancements in the synthesis and application of carbon-based catalysts in the ORR. Electrochem 3:1–27. https://doi.org/10.3390/electrochem3010001
32. Khan S, Yang Z, Yang S, Tang Y, Guo X, Yu F (2025) Porous carbon from ZnCl2 -activated biomass: catalytic performance and

structural insights in ORR. J Chin Chem Soc 72:306–16. https://doi.org/10.1002/jccs.202400334
33. Xia D, Tan F, Zhang C, Jiang X, Chen Z, Li H et al (2016) ZnCl2 -activated biochar from biogas residue facilitates aqueous As(III) removal. Appl Surf Sci 377:361–9. https://doi.org/10.1016/j.apsusc.2016.03.109
34. Thommes M, Kaneko K, Neimark AV, Olivier JP, Rodriguez-Reinoso F, Rouquerol J et al (2015) Physisorption of gases, with special reference to the evaluation of surface area and pore size distribution (IUPAC technical report). Pure Appl Chem 87:1051–69. https://doi.org/10.1515/pac-2014-1117
35. El Azrak A, Grekov DI, Truche L, Pré P (2024) Advanced analysis of clay microporosity using high-resolution N2-Ar adsorption isotherms coupled with the derivative isotherm summation method. Molecules 29:6019. https://doi.org/10.3390/molecules29246019
36. Netto AM, Nascimento MCGM, De Caux LS, Cortez MDOB, Ferreira JPR, Monteiro KA et al (2025) Tertiary treatment of pulp industry effluents using activated biochar derived from biological sludge within a circular economy framework. Processes 13:1647. https://doi.org/10.3390/pr13061647
37. Peres CB, Morais LCD, Resende PMR (2024) Carbon adsorption on waste biomass of passion fruit peel: a promising machine learning model for CO2 capture. J CO2 Util 80:102680. https://doi.org/10.1016/j.jcou.2024.102680
38. Maia AAD, De Morais LC (2016) Kinetic parameters of red pepper waste as biomass to solid biofuel. Bioresour Technol 204:157–63. https://doi.org/10.1016/j.biortech.2015.12.055
39. Gowthami D, Sharma RK, Khalid M, Ismail MY (2024) Enhancing surface properties of circular carbon biochar derived from spent coffee beans through ZnCl2/KOH activation. Bioenerg Res 18:2. https://doi.org/10.1007/s12155-024-10809-5
40. Zhou T, Deng J, Zeng Y, Liu X, Song B, Ye S et al (2024) Biochar meets single-atom: a catalyst for efficient utilization in environmental protection applications and energy conversion. Small 20:2404254. https://doi.org/10.1002/smll.202404254
41. Machado Netto A, Ferreira R, Monteiro JPA, De Lima KS, Varejão COS, Varejão JV (2025) Optimization of Biochar Synthesis from Cosmetic Industry Sludge for Enhanced Removal of Enrofloxacin. J Braz Chem Soc. https://doi.org/10.21577/0103-5053.20250097
42. Fornari MR, Hryniewicz BM, Matos TTS, Schultz J, Vidotti M, Mangrich AS (2025) Graphene-like biochars from pyrolysis of sugarcane bagasse and exhausted black acacia bark for the production of supercapacitors. Biomass Bioenergy 193:107567. https://doi.org/10.1016/j.biombioe.2024.107567
43. Da Silva KS, Cortez MDOB, Mazzini LFM, Favero UG, Rodrigues LDN, Da Silva RC et al (2025) Sustainable hydrochar from orange peel and bagasse: a wet pyrolysis approach for efficient Fe2+and Mn2+removal from water using a factorial design. Processes 13:2040. https://doi.org/10.3390/pr13072040
44. Lu X, Wang J, Peng W, Li N, Liang L, Cheng Z et al (2023) Electrocatalytic hydrogenation of phenol by active sites on Pt-decorated shrimp shell biochar catalysts: performance and internal mechanism. Fuel 331:125845. https://doi.org/10.1016/j.fuel.2022.125845
45. Netto AM, De Oliveira Brahim Cortez M, Rodrigues Ferreira JP, Da Silva RC, Rodrigues N, De Moura Guimarães L et al (2026) Sustainable conversion of pulp industry sludge into activated biochar for high-performance Methylene Blue removal. ACS Omega acsomega.5c09623. https://doi.org/10.1021/acsomega.5c09623
46. Köseoğlu E, Akmil-Başar C (2015) Preparation, structural evaluation and adsorptive properties of activated carbon from agricultural waste biomass. Adv Powder Technol 26:811–818. https://doi.org/10.1016/j.apt.2015.02.006
47. Wu F, Zeng L, Pei A, Feng Y, Zhu L (2024) Pt-on-CoNi alloy nanoparticles supported on N and P co-doped graphene catalyst for highly efficient hydrogen evolution by acidic water electrolysis. Int J Hydrog Energy 63:1128–1136. https://doi.org/10.1016/j.ijhydene.2024.03.138
48. Silva De Souza NC, Olímpio BR, Dias GDC, Gomes JP, Alves De Oliveira KL, Astruc D et al (2025) Sustainable hydrogen production via NH_3 BH_3 hydrolysis using platinum nanoparticles decorated on solvent-free synthesized $LiNbWO_6$. RSC Adv 15:36127–36. https://doi.org/10.1039/D5RA04670J
49. Ullah S, Yuee C, Ahmad I, Ahmad M, Iqbal S (2026) Fabricating ZnO/In2O3 S-scheme heterojunction photocatalyst for increased H2 production performance. J Photochem Photobiol A Chem 474:117001. https://doi.org/10.1016/j.jphotochem.2025.117001
50. Kumar T, Jujjavarapu SE (2026) Smart nanostructured electrodes integrated with microbial fuel cells for wastewater-to-energy conversion and on-site detection of antibiotic in real wastewater. Bioelectrochemistry 169:109211. https://doi.org/10.1016/j.bioelechem.2025.109211
51. Li J, Chen C, Sun Q, Liu J, Xie J, Wang T et al (2026) Constructing Ni single atom and nitrogen vacancies atomic interfacial active sites for synergistic hydrogen evolution coupled with selective benzyl alcohol oxidation. Appl Catal B Environ 385:126293. https://doi.org/10.1016/j.apcatb.2025.126293
52. Jiang J, Wei W, Ren Z, Luo Y, Wang X, Xu Y et al (2023) Facile construction of robust Ru-Co3O4 Mott-Schottky catalyst enabling efficient dehydrogenation of ammonia borane for hydrogen generation. J Colloid Interface Sci 646:25–33. https://doi.org/10.1016/j.jcis.2023.04.181
53. Doherty S, Knight JG, Alharbi HY, Paterson R, Wills C, Dixon C et al (2022) Efficient hydrolytic hydrogen evolution from sodium borohydride catalyzed by polymer immobilized ionic liquid-stabilized platinum nanoparticles. ChemCatChem 14:e202101752. https://doi.org/10.1002/cctc.202101752
54. Demirci UB, Miele P (2014) Reaction mechanisms of the hydrolysis of sodium borohydride: A discussion focusing on cobalt-based catalysts. C R Chim 17:707–716. https://doi.org/10.1016/j.crci.2014.01.012
55. Paterson R, Alharbi AA, Wills C, Dixon C, Šiller L, Chamberlain TW et al (2022) Heteroatom modified polymer immobilized ionic liquid stabilized ruthenium nanoparticles: efficient catalysts for the hydrolytic evolution of hydrogen from sodium borohydride. Mol Catal 528:112476. https://doi.org/10.1016/j.mcat.2022.112476
56. Sermiagin A, Meyerstein D, Rolly GS, Mondal T, Kornweitz H, Zidki T (2022) Mechanistic implications of the solvent kinetic isotope effect in the hydrolysis of NaBH4. Int J Hydrog Energy 47:3972–3979. https://doi.org/10.1016/j.ijhydene.2021.11.040
57. Liu S, CHEN X, Ren W, Feng J, Hao, Wang X et al (2025) Preparation of supported Ru/CN catalysts and their performance in hydrogen generation from the catalytic hydrolysis of ammonia borane. Chin J Eng 47:1047–1054
58. Akbayrak S, Tanyıldızı S, Morkan İ, Özkar S (2014) Ruthenium(0) nanoparticles supported on nanotitania as highly active and reusable catalyst in hydrogen generation from the hydrolysis of ammonia borane. Int J Hydrog Energy 39:9628–9637. https://doi.org/10.1016/j.ijhydene.2014.04.091
59. Zhang Q, Fang C, Wang Y, Liu X (2024) Selective and efficient H2 evolution upon NH3BH3 hydrolysis at subzero temperatures. iScience 27:108774. https://doi.org/10.1016/j.isci.2023.108774

Publisher's note Springer Nature remains neutral with regard to jurisdictional claims in published maps and institutional affiliations.

Authors and Affiliations

Antonio Machado Netto[1] · Mariele Dalmolin da Silva[2] · Marcela de Oliveira Brahim Cortez[1] · Gessica do Carmo Dias[1] · Bárbara Fernandes de Souza[1] · Guilherme Mateus Bousada[1] · Renata Pereira Lopes Moreira[1]

✉ Renata Pereira Lopes Moreira
renata.plopes@ufv.br

[1] Departament of Chemistry, Universidade Federal de Viçosa (UFV), Av. Peter Henry Rolfs, s/n, Campus Universitário, Viçosa 36570-900, MG, Brasil

[2] Department of Agricultural Engineering, Universidade Federal de Viçosa (UFV), Av. Peter Henry Rolfs, s/n, Campus Universitário, Viçosa 36570-900, MG, Brasil